


Reduced bacterial adhesion on zirconium-based bulk metallic glasses by femtosecond laser nanostructuring

Proc IMechE Part H:
J Engineering in Medicine
2020, Vol. 234(4) 387–397
© IMechE 2019
Article reuse guidelines:
sagepub.com/journals-permissions
DOI: 10.1177/0954411919898011
journals.sagepub.com/home/pih


Cezhi Du, Chengyong Wang, Tao Zhang, Xin Yi,
Jianyi Liang and Hongjian Wang 

Abstract

As high-performing materials, bulk metallic glasses have attracted widespread attention for biomedical applications. Herein, the bacterial adhesion properties of femtosecond laser-nanostructured surfaces of four types of zirconium-based bulk metallic glasses are assessed. Laser-induced periodical surface structures and nanoparticle structures were fabricated by femtosecond laser irradiation under different energy intensities (0.23 and 2.3 J/mm²). Surface topography, roughness, wettability, and surface energy were investigated after femtosecond laser irradiation and the surface bacterial adhesion properties were explored using *Escherichia coli* and *Staphylococcus aureus* as respective representatives of Gram-negative and Gram-positive bacteria. 4',6-Diamidino-2-phenylindole fluorescence staining was used to characterize and assess the bacterial surface coverage rate. The *in vitro* cytotoxicity of polished and laser-nanostructured surfaces was investigated using MC3T3-E cells. The obtained results demonstrate that femtosecond laser surface nanostructuring retained the amorphous structure of zirconium-based bulk metallic glasses and led to an obvious decrease in bacterial adhesion compared with polished surfaces. The inhibition of bacterial adhesion on laser-induced periodical surface structures was greater than on nanostructured surfaces after 24 h of bacterial incubation. In addition, femtosecond laser nanostructuring did not have an apparent effect on the cytotoxicity of zirconium-based bulk metallic glasses.

Keywords

Bacterial adhesion, bulk metallic glass, femtosecond laser, nanostructure

Date received: 5 June 2019; accepted: 9 December 2019

Introduction

Bulk metallic glasses (BMGs), also known as amorphous alloy or liquid metals, have received increasing attention in recent years given their wide field of potential applications such as in medical devices, sensors, and nanotechnology, among others.^{1,2} The unique nanostructures of BMGs, with internal atoms showing both short-range order and long-range disorder, exhibit high fracture toughness, low elastic moduli, good corrosion resistance, and super-plasticity.^{3–5} These properties have been confirmed as superior to those of common biomedical materials such as stainless steel, pure titanium, and titanium alloys.^{2,6} Based on the excellent properties, the BMG medical devices such as scalpel, arthroscopic shaver, syringe needle will show its advantages to traditional metal devices. Therefore, the corrosion behavior, biocompatibility, biodegradability, and critical size of various BMGs have been extensively investigated with the aim of applying these materials as potential medical devices.^{2,6–10}

Bacterial contamination and colonization on material surfaces greatly affect patient health and the treatment effect of medical devices. In clinical infection cases, unqualified sterilization of medical devices is closely related to medical infections.¹¹ Bacterial infection rates can increase to 40% without the use of antibiotic use on the post-operative surgical site.¹² The first step in bacterial contamination and colonization is bacterial adhesion.¹³ Therefore, the antibacterial adhesion properties of medical devices play a major role in decreasing bacterial infection during clinical treatment.¹⁴ With this in mind, the bacterial adhesion properties of biomaterials, including the effect of surface

School of Electromechanical Engineering, Guangdong University of Technology, Guangzhou, China

Corresponding author:

Chengyong Wang, School of Electromechanical Engineering, Guangdong University of Technology, Guangzhou 510006, China.
Email: cywang@gdut.edu.cn

Table 1. Material composition and physical properties of Zr-BMGs.

Specimen mark	Element content	Vickers hardness (HRC)	Young's modulus (GPa)	Critical thickness (mm)
V105s	Zr _{43.3} Cu _{27.8} Ni _{15.2} Al _{9.1} Ti _{4.6}	532	89.3	< 3.5
V105	Zr _{57.5} Cu _{21.1} Ni _{14.2} Al _{3.7} Ti _{3.5}	563	88.2	< 3
106c	Zr _{63.2} Cu _{21.4} Ni _{11.3} Al _{4.1}	530	86.9	< 3.5
Zum	Zr _{58.9} Cu _{33.2} Ni _{4.2} Al _{3.7}	582	90.2	< 4

topography, wettability, functional groups, and anti-bacterial elements, have been extensively studied.¹⁵ Surface nanostructuring was shown to decrease surface bacterial adhesion,¹⁶ with nanostructures having a surface topography interval smaller than bacterial dimensions leading to a change in bacterial contact status on the material surface and obviously decreasing the bacterial adhesion rate.^{17,18} Antibacterial coatings composed of Ag, Cu, or Zn have also been shown to be effective in decreasing bacterial adhesion.^{19,20} Furthermore, superhydrophobic surfaces with a low surface energy have been shown to decrease the contact rate of bacteria.²¹ However, for metal surfaces, superhydrophobicity is usually achieved by surface functionalization, which affects the durability of hydrophobicity. Superhydrophilic surfaces with a negative zeta potential exhibit limited bacterial binding and can also decrease bacterial adhesion rates.^{22,23}

Surface nanostructure modification can be achieved through various methods, including photoetching,²⁴ patterning,²⁵ ultrafast laser irradiation,²⁶ and focused ion beam.²⁷ Polyethylene terephthalate surfaces with micropatterning on a length scale comparable with bacterial dimensions had a significant effect on *Escherichia coli* adhesion behavior.²⁸ The study of bacterial adhesion properties of focused ion beam-nanostructured poly(ethylene glycol) hydrogel surfaces showed that *Staphylococcus epidermidis* cells did not adhere effectively when the length scale of the nanostructure was comparable with the cell size.²⁹ Femtosecond laser irradiation is a cold processing and surface nanostructuring technology with properties of non-contact processing model and high processing efficiency, widely used for temperature-sensitive material processing.³⁰ The use of femtosecond laser irradiation avoided the crystallization of BMGs during laser irradiation.³¹ Furthermore, the bacterial adhesion properties on femtosecond laser-induced nanostructured titanium alloy and 45S5 bioactive glass biomaterials were shown to be effectively decreased.^{32,33}

This study aims to investigate the bacterial adhesion properties of femtosecond laser-induced nanostructured zirconium-based bulk metallic glasses (Zr-BMGs) in relation to the application of antibacterial metallic glass medical devices. Four types of Zr-BMGs were selected to investigate the difference in antibacterial properties and *in vitro* cytotoxicity. *E. coli* and *S. aureus*, as representatives of Gram-negative and Gram-positive bacteria, respectively, were selected to assess

the antibacterial properties of Zr-BMGs after femtosecond laser nanostructuring and MC3T3-E1 pre-osteoblastic cells were used to examine the surface cytotoxicity of the material surfaces.

Materials and methods

Material preparation

Four types of Zr-BMGs (V105s, V105, 106c, and Zum) with different composition elements and content were used herein. The Zr-BMGs have varying physical properties (Table 1). Furthermore, the hardness, Young's modulus, and critical thickness of materials are important parameters for the potential application of Zr-BMGs as medical devices.² Zr-BMG ingots were provided by EONTEC and were produced by vacuum die casting. The specimen size was 10 mm × 10 mm × 1 mm (length, width, and thickness). The surface roughness (R_a) of the four BMGs was within the 0.01–0.02 μm range after the polishing process prior to laser irradiation. The specimens were cleaned four times in absolute ethyl alcohol for 30 min at 40 °C in ultrasonic bath after the polishing process and dried at 60 °C.

Surface nanostructuring

A femtosecond laser beam was produced by a laser device (Pharos PH1-10) at a wavelength of 1030 nm, with a 200-fs pulse width and 100-KHz ablation frequency. The focused laser beam was approximately 35 μm in diameter with a field lens of 160 mm focal length. The single pulse energy was selected at 40 μJ to fabricate the surface nanostructures. The laser scanning intervals were of 10 μm . Laser-induced periodical surface structure (LIPSS) and nanoparticle structures were achieved under low energy intensity (0.23 J/mm²) with 500 mm/s scanning speed and high energy intensity (2.3 J/mm²) with 50 mm/s scanning speed, respectively, in air. The energy intensity was calculated using equation³⁴

$$I = \frac{P}{v * \varnothing} \text{ J/mm}^2 \quad (1)$$

where I was laser energy intensity, P was laser power, v was scanning speed, \varnothing was the diameter of laser beam. The femtosecond laser-nanostructured area was 8 mm × 8 mm.

Table 2. Liquid surface energy.

Liquid	γ_L^D (mJ/m ²)	γ_s^P (mJ/m ²)	Type
Water	21.8	51	Polar
n-Hexadecane	27.6	0	Nonpolar

After the laser irradiation process, the specimens were cleaned in ultrasonic bath with absolute ethyl alcohol for 30 min at 40°C and then in sterile deionized water for 20 min at 40°C to remove the surface residual dust deposited during the laser irradiation process. Scanning electron microscopy (Hitachi SU8220), atomic force microscopy (Bruker Dimension FastScan), and atomic-profiler (Kosaka ET-150) were used to examine the surface topography and roughness before and after laser irradiation. X-ray diffraction (XRD) measurements were used to examine the surface structure layer after laser irradiation with 1° incident angle. The sessile drop method was used to evaluate the surface wettability of specimens. A contact angle goniometer (OSA-200) was used to examine the contact angle after water drop loading. To evaluate the surface energy by Owens two-liquid method, deionized water and n-hexadecane were used to test the specimen surface contact angle. Surface energy of each specimens were calculated using equations (2) and (3)³⁵

$$\gamma_s = \gamma_s^D + \gamma_s^P \quad (2)$$

$$\gamma_L(1 + \cos\theta) = 2(\gamma_s^D \gamma_L^D)^{1/2} + 2(\gamma_s^P \gamma_L^P)^{1/2} \quad (3)$$

γ_s is surface free energy of the specimen; γ_s^D is the dispersion force of specimen, and γ_s^P is the polar force of specimen. θ is the contact angle; γ_L^D is the dispersion force of liquid, and γ_L^P is the polar force of liquid. The liquid surface energy of water and n-hexadecane were shown in Table 2.

Bacterial attachment

Prior to bacterial incubation, the specimens were autoclaved at 121°C under 0.1 MPa after the surface cleaning process and placed into six-well cell culture plates with the polished and laser-nanostructured surface facing upward. Bacterial incubation and adhesion tests were performed at the Guangdong Institute of Microbiology. *E. coli* (AS1.0.2385) and *S. aureus* (ATCC 6538) were selected as representatives of Gram-negative and Gram-positive bacteria, respectively, to assess the bacterial adhesion properties of the specimens. Bacteria were grown for 24 h from a frozen stock in Luria–Bertani (LB) broth at 37°C to achieve the logarithmic phase of bacterial growth. Following the preincubation process, the concentration of bacteria

was adjusted to 10⁷ CFU/mL and 5 mL of the respective bacterial solutions were added into each well. Cell culture plates were placed in a cell incubator and cultured for 24 h with a revolving speed of 100 r/min at 37°C. After 24 h of bacterial incubation, the specimens were retrieved and washed three times with 3 mL of phosphate buffer saline (PBS) solution at 100 r/min for 5 min, and then fixed with a 4% paraformaldehyde suspension. 4',6-Diamidino-2-phenylindole (DAPI) fluorescence was used to stain the bacterial nuclei. After fluorescence staining, specimens were washed in sterile deionized water three times and dried at 25°C. Fluorescence microscopy (Axio Imager A2, ZEISS) was used to examine the surface coverage morphology of bacteria, whereas the bacterial surface coverage rate was evaluated by gray analysis of the fluorescence microscopy image using Image J software.

In vitro cytotoxicity evaluation

The *in vitro* cytotoxicity was evaluated using MC3T3-E1 pre-osteoblastic cells. Cell suspensions were prepared in a minimum essential medium (MEM) with 10% fetal bovine serum (FBS). A 0.5-mL aliquot of the cell suspension at a concentration of 2 × 10⁴ cells/mL was seeded onto the specimen surface and incubated at 37°C in a 5% CO₂ humidified atmosphere for 24 h. A cholecystokinin (CCK)-8 test was used to evaluate the cell viability. The optical density (OD) values of each well was measured by a spectrophotometer (TriStar2S LB942) at 450 nm. Cell viability was determined by the following formula

$$\text{Viability} = \frac{(OD_{\text{sample}} - OD_{\text{blank}})}{(OD_{\text{control}} - OD_{\text{blank}})} \times 100\% \quad (4)$$

After 24-h incubation, the specimens were washed three times with 3 mL of PBS and fixed in a 4% paraformaldehyde suspension. Fixated cells were stained by DAPI fluorescence for 15 min, then washed in PBS three times, and dried in air at 25°C in the dark. The research approach is illustrated in Figure 1.

Statistical analysis

Surface characterization was performed in duplicate for each surface type. R_a and contact angle were measured three times for each specimen. Values in all graphs are reported as mean ± standard deviation. The bacterial surface area coverage rate and surface cell viability evaluations were repeated three times for each bacteria/cell type, with at least three images per sample. Statistical analysis was performed using one-way analyses of variance (ANOVAs) to evaluate the differences between each case and results were considered statistically significant at a p value of less than 0.05.

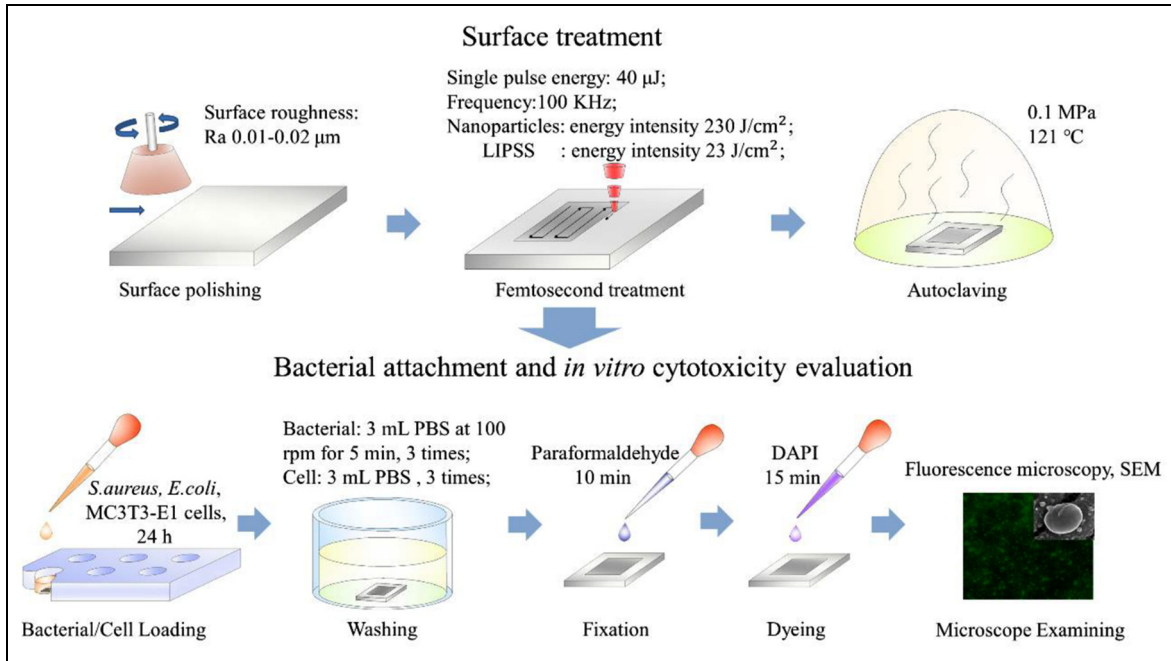


Figure 1. Research approach schematic.

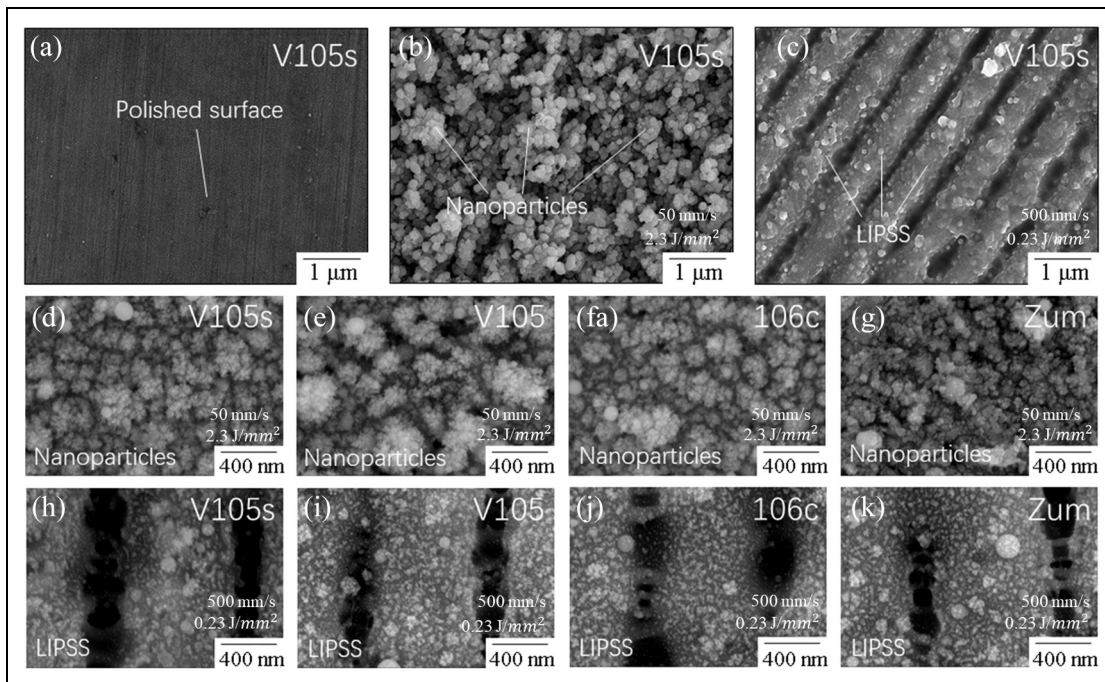


Figure 2. Morphology of femtosecond laser-nanostructured surface: (a) polished surface of V105s; (b) nanoparticle structure surface of V105s; (c) LIPSS of V105s; (d–g) nanoparticle structure surface of Zr-BMGs; and (h–k) LIPSS of Zr-BMGs.

Results and discussion

Surface morphology

The surface morphology of Zr-BMGs was assessed after femtosecond laser irradiation at an energy density

of 0.23 and 2.3 J/mm^2 (Figure 2). The polished surface of V150s showed shallow nanoscale scratches induced by the mechanical polishing process (Figure 2(a)), with no obvious bulge; XRD indicated an amorphous phase as observed by a diffuse peak (Figure 3). Following

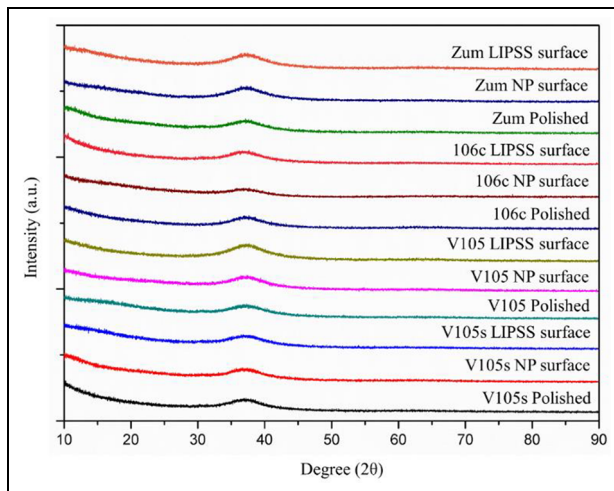


Figure 3. Surface XRD pattern of specimens after polishing and laser irradiation.

high-energy intensity (2.3 J/mm^2) laser irradiation on the BMG surface, the surface was covered with a disordered distribution of nanoparticles formed via surface plasma deposition under high laser energy intensity (Figure 2(b)).³⁶ Conversely, laser irradiation at low-energy intensity (0.23 J/mm^2) and $10 \mu\text{m}$ scanning intervals led to the formation of LIPSS with a periodicity of 800 nm (Figure 2(c)). The periodicity of LIPSS is determined by the laser wavelength and material wavelength-dependence dielectric constant.³⁷ These three-dimensional (3D) periodical nanoarrays were also covered by nanoparticles (Figure 2(c), (h)–(k)). The surface morphology clearly indicates that no obvious differences in morphology were observed between the four Zr-BMG material surfaces under the same irradiation energy intensity (Figure 2).

XRD measurements showed that the diffuse peak of the polished and laser-nanostructured surfaces did not change following the irradiation process (Figure 3). This is as expected since the ultra-short duration pulse did not allow heat transformation; indeed, the laser pulse duration time was of approximately 200 fs , which is far less than lattice heat transfer velocity.³⁸ Therefore, femtosecond laser processing retained the surface amorphous structure of Zr-BMGs.

Surface roughness

Surface morphology is an important factor influencing surface bacterial adhesion.¹⁵ With regards to the nanoscale topography of specimen surfaces, the intervals between nanoparticles or nanoarrays decrease the bacterial contact area when at a scale smaller than bacterial cell size. Therefore, the surface roughness (R_a) was examined by atomic force profiling and atomic force microscopy (Figure 4(a)). The polished surface had a relatively smooth surface, with minimal cross-section profile variation on the 1 mm scan scale (Figure 4(a)). The microscale roughness of all polished surfaces varied between 0.068 ± 0.02 and $0.079 \pm 0.03 \mu\text{m}$.

Furthermore, the microscale roughness of the nanoparticle surfaces (varying between 0.435 ± 0.06 and $0.482 \pm 0.08 \mu\text{m}$) was higher than that of the LIPSS (varying between 0.119 ± 0.04 and $0.142 \pm 0.03 \mu\text{m}$) due to the deeper laser scanning grooves achieved with the higher irradiation energy intensity, yet the roughness variation between each specimen with the same morphology was small (Figure 4(b)). For the nanoscale morphology of the laser-nanostructured surface, the surface profile variation of nanoparticle structures was less than for LIPSS (Figure 4(c)). The polished surfaces had a minimum roughness (varying between 12.2 ± 4.2 and $17.4 \pm 3.6 \text{ nm}$) in nanoscale measurement while that of the LIPSS (varying between 64.1 ± 9.1 and $73.2 \pm 7.7 \text{ nm}$) were higher than for the nanoparticle surfaces (varying between 46.3 ± 4.2 and $54.5 \pm 3.8 \text{ nm}$). LIPSS of approximately 50 nm in depth and with a periodicity of 800 nm were generated during femtosecond laser irradiation, which caused a higher nanoroughness than in other surfaces. The nanoscale roughness variation between specimens with the same morphology was also small (Figure 4(d)).

Surface contact angle and surface energy

To evaluate the surface energy based on the Owens two-liquid method, deionized water was selected to evaluate the surface contact angle of polar liquid and n-hexadecane was selected to evaluate the surface contact angle of nonpolar liquid. The contact angle was measured for each surface after laser irradiation and ultrasonic cleaning in absolute ethyl alcohol. The water contact angle decreased obviously on laser-nanostructured surface compared with polished surface while n-hexadecane contact angle variation tendency was similar to water contact angle, but the n-hexadecane contact angle were smaller than water contact angle with the same surface morphology and material (Figure 5(a)). For the polished surfaces of all Zr-BMGs, the water contact angle variation was obvious (Figure 5(b)). The polished V105s had the highest contact angle (approximately $73.1^\circ \pm 2.2^\circ$) while Zum had the smallest contact angle (approximately $59.7^\circ \pm 1.4^\circ$). However, following femtosecond laser irradiation, the surface contact angles decreased for all materials. For example, the contact angle of polished 106c was approximately $65.8^\circ \pm 1.7^\circ$, while after laser irradiation, the surface contact angle decreased to $31.5^\circ \pm 1.2^\circ$ (nanoparticle surface) and $35.7^\circ \pm 1.3^\circ$ (LIPSS). Furthermore, a minimal increase in the contact angle was observed for the LIPSS compared with that of the nanoparticle-structured surface, with the nanoparticle-structured surface showing the highest hydrophilicity. Comparing the four types of BMGs with the similar surface morphology, V105 showed the most hydrophobic properties with both the polished surface and LIPSS, yet for the nanoparticle-structured surface, Zum was the most hydrophilic. But the differences of hydrophilicity between four Zr-BMGs with laser-

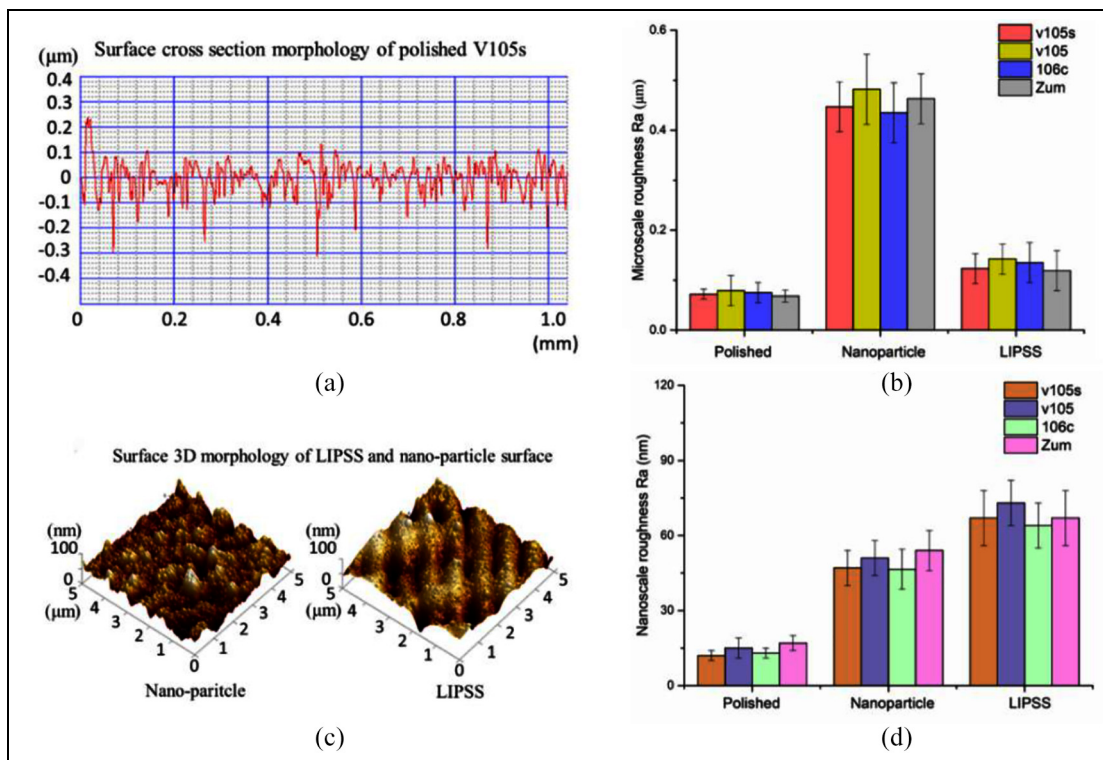


Figure 4. (a) Surface cross-section morphology, (b) microscale roughness variation of specimens, (c) 3D nanomorphology of nanostructured surface, and (d) nanoscale roughness variation of specimens.

nanostructured surfaces were inapparent. The surface contact angle of n-hexadecane was obviously decreased compared with water as shown in Figure 5(c). For example, the n-hexadecane contact angle of V105s was only $17.3^\circ \pm 1.1^\circ$ (polished surface), $5.2^\circ \pm 0.5^\circ$ (nanoparticle surface), and $9.3^\circ \pm 0.7^\circ$ (LIPSS). Surface energy variation tendency was inversely proportional to contact angle as shown in Figure 5(d). The surface energy of polished surface (variation between 36.8 ± 1.3 and $45.1 \pm 1.0 \text{ mJ/m}^2$) were smaller than nanostructured surfaces. Meanwhile, for nanostructured specimens, nanoparticle surface (surface energy variation between 61.0 ± 1.1 and $64.0 \pm 0.9 \text{ mJ/m}^2$) with smaller contact angle got the highest surface energy compared with LIPSS (surface energy variation between 57.8 ± 0.9 and $61.9 \pm 0.8 \text{ mJ/m}^2$).

Surface bacterial adhesion

The *E. coli* and *S. aureus* surface coverage morphology was observed under fluorescence microscopy after DAPI staining (Figure 6(a) and (b)). The surface bacterial coverage rate of specimens was calculated via gray analysis of fluorescence microscopy images (Figure 6(c)). The all polished surfaces with maximal contact angle and minimal surface roughness showed maximum bacterial attachment after 24 h of incubation for both *E. coli* and *S. aureus*. It was found that the *E. coli* coverage rate of all polished surfaces varied between $10.1\% \pm 1.3\%$ and $15.2\% \pm 1.7\%$. Furthermore,

comparing the four types of Zr-BMGs, V105s exhibited minimal bacterial attachment, with a surface coverage rate of $10.1\% \pm 1.3\%$, while the other Zr-BMGs varied between $13.4\% \pm 1.5\%$ and $15.2\% \pm 1.7\%$ for *S. aureus* surface coverage. In addition, surface coverage for all polished surfaces varied between $16.8\% \pm 2.1\%$ and $21.3\% \pm 1.9\%$, with V105s also showing minimal bacterial attachment ($16.8\% \pm 2.1\%$) while Zum had the highest coverage ($21.3\% \pm 1.9\%$). The nanoparticle surfaces and LIPSS exhibited obvious antibacterial adhesion properties, as determined by a decrease in bacterial coverage rate. The surface coverage rate of *E. coli* on all nanoparticle surfaces varied between $5.4\% \pm 0.9\%$ and $9.7\% \pm 0.7\%$, while that of *S. aureus* varied between $9.3\% \pm 1.5\%$ and $11.5\% \pm 1.2\%$. However, all LIPSS showed minimal bacterial attachment for both *E. coli* and *S. aureus*. The *E. coli* surface coverage rate varied between $3.1\% \pm 0.7\%$ and $6.5\% \pm 0.5\%$, while that of *S. aureus* varied between $3.6\% \pm 0.6\%$ and $9.1\% \pm 0.5\%$. Compared with the femtosecond laser-nanostructured surfaces of all Zr-BMGs, the surface coverage rate for both bacteria was slightly higher on the nanostructured Zum surfaces than on the other Zr-BMGs, while V105s exhibited the lowest bacterial adhesion rate.

Bacterial adhesion mechanism

When specimens are immersed in bacterial solutions (Figure 1), the floating bacteria undergo Brownian

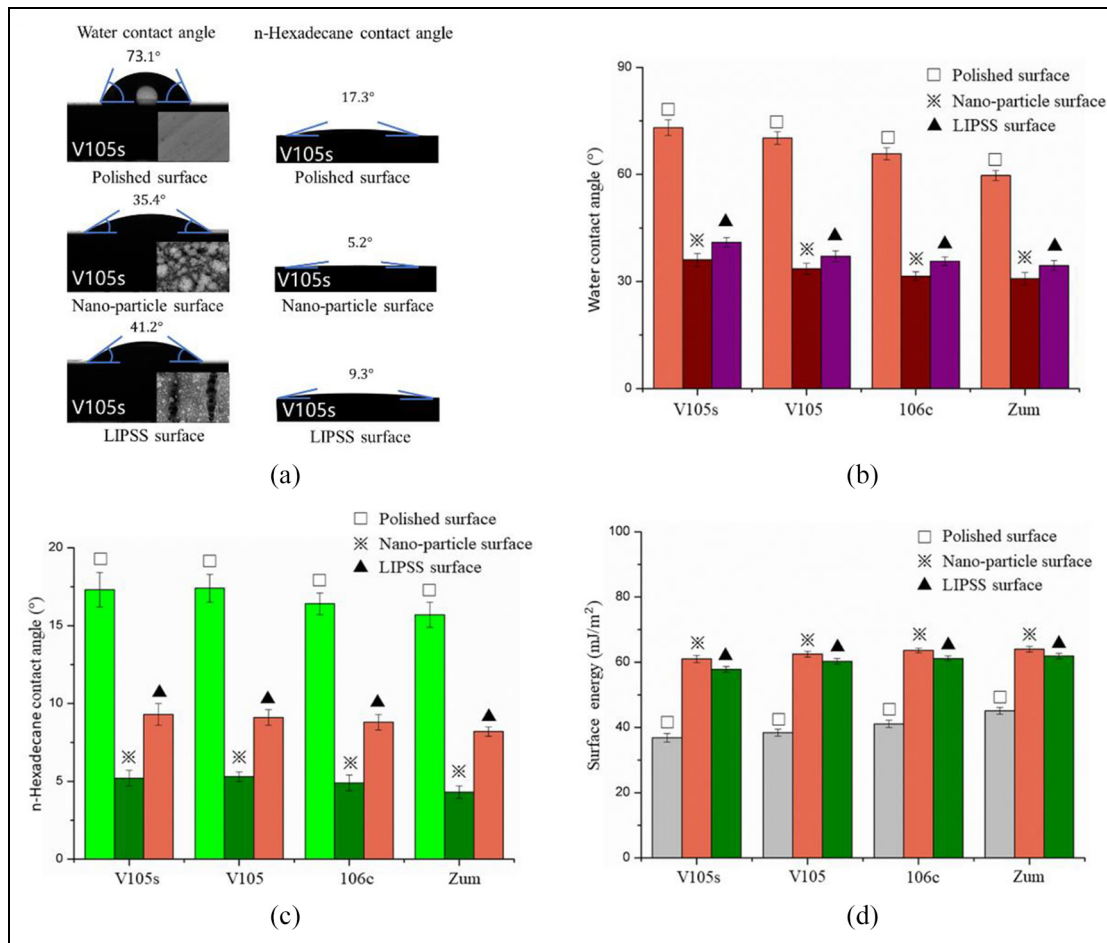


Figure 5. (a) Contact angle variation of V105s surfaces with different structures, (b) water contact angle variation of specimens, (c) n-hexadecane contact angle variation of specimens, and (d) surface energy variation of specimens; error bars represent the standard deviations based on three measurements of different areas on each specimen.

motion until they come within the proximity of a metal surface.³⁹ Floating bacteria are then attracted to the metal when the distance between the bacterial surface and the metal surface is less than the Coulomb force; this process may include physical and chemical reactions.⁴⁰ The extended Derjaguin–Landau–Verwey–Overbeek (XDLVO) theory using the Van der Waals force, polar interactions, electrical double layer interactions, and Brownian motion forces can be employed to explain the total free energy between two surfaces during the bacterial adhesion process. The XDLVO theory assumes that bacteria are colloid particles with a particle size ranging from 0.5 to 2 μm, as shown in equation (5)⁴¹

$$\Delta G^{TOT} = \Delta G^{LW} + \Delta G^{AB} + \Delta G^{DL} + \Delta G^{BR} \quad (5)$$

where ΔG^{LW} is the Van der Waals force, ΔG^{AB} is the polar interaction, ΔG^{DL} is the Coulomb force, and ΔG^{BR} is Brownian motion force. Van der Waals forces are affected by distance between two surfaces. Under the same incubation conditions, the Brownian motion

forces between each surface are nearly identical, yet the polar interactions and electrical double layer interactions are decided by surface topography, surface charge, and surface composition.

The Van der Waals forces act when bacteria are in close proximity to the surface, with the process being irreversible. The Coulomb force acts at a distance from the surface, when the Van der Waals force has little effect. Coulomb forces are related to surface charge, caused by surface ionic groups and free charges.⁴² Metal surfaces are commonly positively charged, while bacterial surfaces are negatively charged.⁴³ Based on the XDLVO theory, the first step of bacterial adhesion is the interaction of Coulomb forces between the metal surface and bacteria. For high surface energy specimens, the Coulomb force is higher than for small surface energy specimens, coupled with stronger polar and electrical double layer interactions. In this case, the laser-nanostructured surfaces attracted bacteria more easily than did polished surfaces when immersed in the bacterial solution, yet the surface topography affected bacterial adhesion.

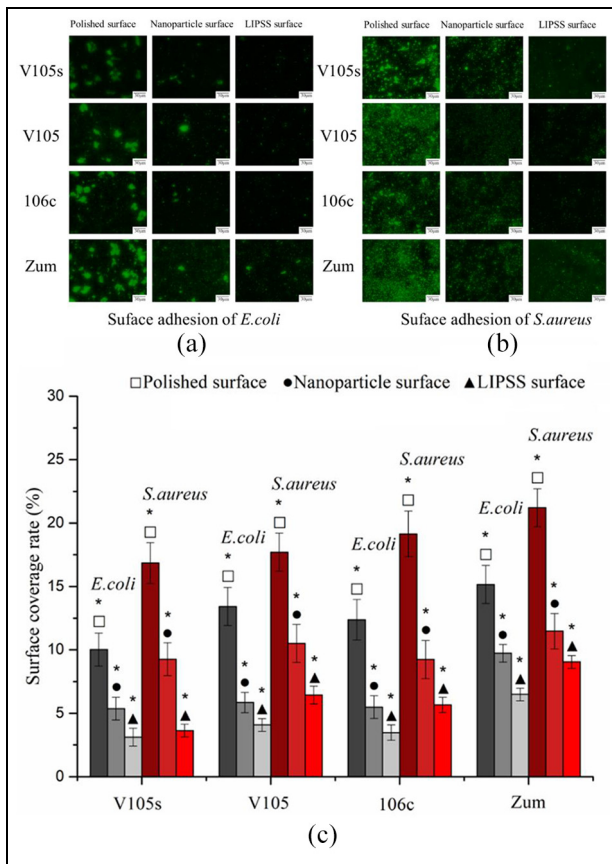


Figure 6. Surface adhesion of *E. coli* and *S. aureus* after 24 h of incubation. Fluorescence microscopy images of (a) *E. coli* and (b) *S. aureus* adhesion on specimen surfaces, and (c) surface bacterial coverage rate of specimens; error bars represent the standard deviations.

* $p < 0.05$.

Surface topography and bacterial adhesion

For nanostructured surfaces, when the maximum curvature radius of the surface structures is smaller than the minimum curvature radius of bacteria, the contact status between bacteria and material are changed.⁴⁴ The cytoderm will fully adhere to a smooth surface without surface bulge support while the cytoderm is lifted by surface nanobulges on nanostructured surfaces, leading to a decreased adhesion area.⁴⁵ Herein, nanostructured surfaces also exhibited antibacterial properties for the four types of Zr-BMGs. To illustrate this, the *S. aureus* contact status on V105s surfaces was closely monitored (Figure 7). A single *S. aureus* was shown to adhere onto the polished surface after 24 h of incubation (Figure 7(a)). Conversely, the *S. aureus* bacterium was lifted by the nanoparticles on the laser-nanostructured surface (Figure 7(b)), while it was also lifted by nanoparticles between the two nanoarrays (Figure 7(c)). To better illustrate this, a schematic of bacterial contact status on polished and laser-nanostructured surfaces is provided (Figure 7(d)–(f)). Given their protein-based cytomembranes and water-based cytoplasm, bacteria act as a viscoelastic body while in contact with metal surfaces.⁴⁶ The cytomembrane of bacteria was fully adhered onto the BMG surface for the attraction between metal surface and bacteria (Figure 7(d)). Bacteria had a greater contact area on a polished surface than on the laser-nanostructured surface (Figure 7(a)–(c)). The existence of nanoparticles and nanoarrays lifted the bacteria and decreased the contact area between the surface and the bacterium. The lack of an adhesion area effectively decreased surface adhesion (Figure 7(e) and (f)). The decrease in contact area in femtosecond laser-nanostructured surfaces seems to do more positive

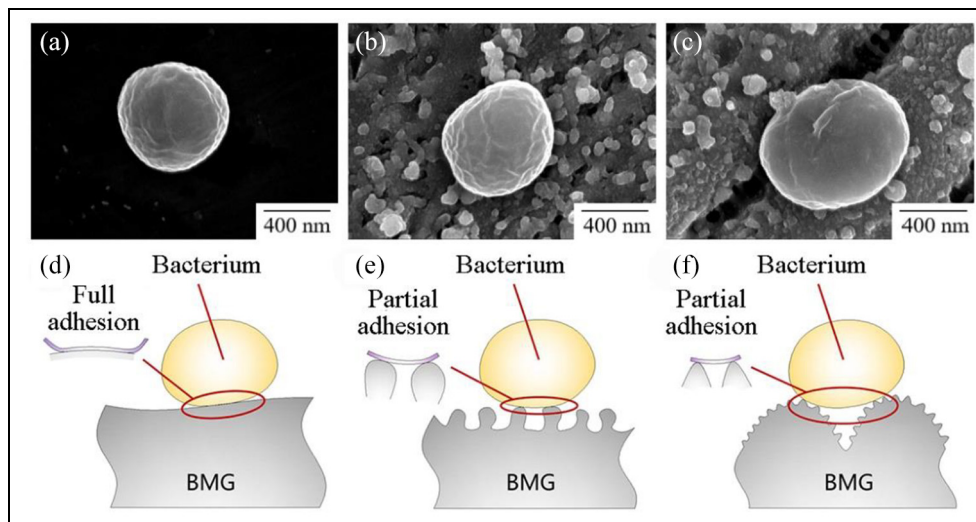


Figure 7. Surface contact status of *S. aureus* on (a) polished surface, (b) nanoparticle structure surface, and (c) LIPSS. Schematic of surface bacterial adhesion status (d) on a polished surface, (e) on a nanostructured surface, and (f) on a LIPSS. Nanoparticle-structured surface.

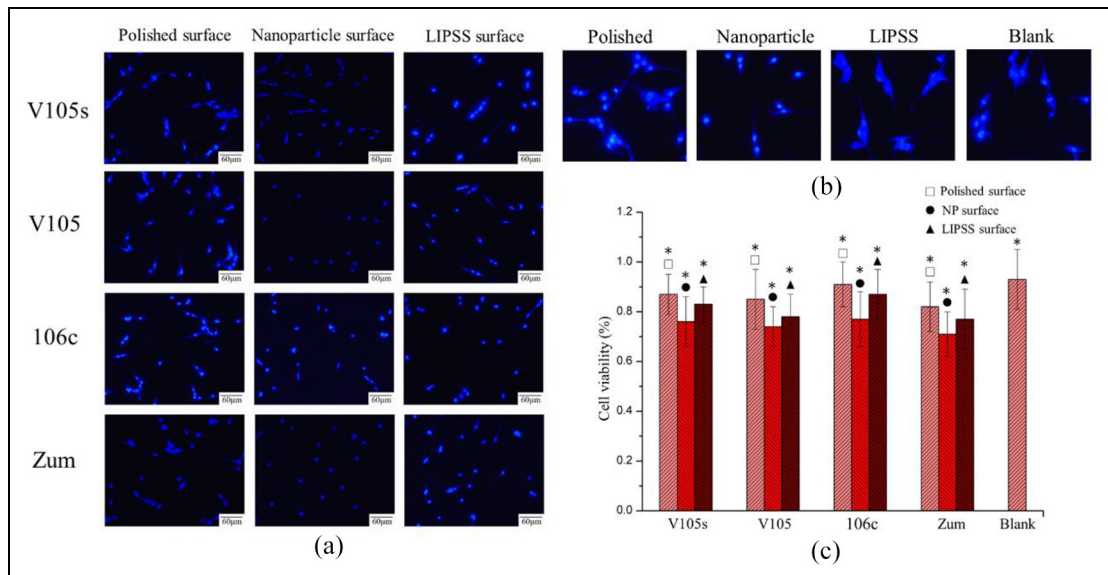


Figure 8. Surface MC3T3-E cell status after 24 h of incubation. (a) Fluorescence microscopy images of MC3T3-E cells on specimen surfaces, (b) MC3T3-E cell spreading status on V105s surface and blank group, and (c) cell viability after 24 h culturing with specimen; error bars represent the standard deviations and * $p < 0.05$.

affection to loose the contact force in spite of surface energy increased. During the PBS washing process, the numbers of bacteria removed with the PBS fluid from the nanostructured surfaces was greater in all polished surfaces with fully adhered status.

Surface in vitro cytotoxicity

Surface nanostructures and material composition can modify the biological performance of materials.⁴⁷ Herein, after 24 h of incubation, MC3T3-E cells were well spread and displayed lateral spreading features with distinct cytoplasmic extension on the polished surfaces of the four Zr-BMGs (Figure 8(a)). However, the MC3T3-E cells did not grow as well as on the nanostructured surfaces. For the LIPSS, MC3T3-E cell activity was better than on the nanostructured surface, showing distinct cytoplasmic extension features. Furthermore, the spreading of MC3T3-E cells on the LIPSS of V105s and V105 were better than for 160c and Zum, with MC3T3-E cells on the 106c surface showing a complete lack of spreading. For MC3T3-E cells growing on V105s (Figure 8(b)), the cell spreading area of the nanostructured surface was smaller than for the polished surface and LIPSS with agglomerates status. The cell spreading status of blank group seems to have little difference to polished and LIPSS. Meanwhile, the cytotoxicity of LIPSS shows little differentiation to polished surface. In addition, the MC3T3-E cell viability cultured after 24 h with each specimens were shown in Figure 8(c). Cells viability of polished surfaces groups varying from $0.82\% \pm 0.09\%$ to $0.91\% \pm 0.1\%$, yet on the laser-nanostructured surface group, the cell viability were showing little more cytotoxicity than the polished. The cell viability cultured with nanoparticle-structured surfaces group varied from

$0.71\% \pm 0.1\%$ to $0.76\% \pm 0.12\%$, while from the LIPSS group, it varied from $0.79\% \pm 0.12\%$ to $0.87\% \pm 0.09\%$. The laser-nanostructured surface of V105s showed a better biological performance than the other three Zr-BMGs with regards to cell spreading status, yet the cell viability were similar for all materials. The surface nanostructures seemed to have shown little cytotoxicity and also affected cell spreading status (Figure 8(b) and (c)).

Conclusion

Herein, four Zr-based materials were selected to examine the bacterial adhesion properties after femtosecond laser irradiation. A laser irradiation energy intensity of 0.23 and 2.3 J/mm² was chosen to form different surface nanostructures. *E. coli* and *S. aureus* were used to examine the bacterial adhesion properties of Gram-negative and Gram-positive bacteria, respectively. The results showed that:

1. The polished surfaces exhibited the highest bacterial adhesion rate for all BMGs under the same incubation conditions.
2. The femtosecond laser-nanostructured surfaces had a decreased bacterial adhesion rate after 24 h incubation compared with that of the polished surfaces.
3. For laser-nanostructured surfaces, the existence of LIPSS decreased the bacterial adhesion rate more than for the nanoparticle-covered surface. The decrease of *E. coli* adhesion rate was more efficient than for *S. aureus* for all specimens.
4. For laser-nanostructured surfaces of Zr-BMGs, the surface morphology and wettability affected the surface bacterial adhesion rate. V105s seemed to

have the best antibacterial adhesion properties at the same surface morphology compared with the other three materials.

5. Laser-nanostructured surfaces were shown to exert minimal cytotoxicity compared with the polished surfaces and the surface cytotoxicity of the LIPSS was less than that of the nanoparticle surface. However, the variation of surface MC3T3-E cell viability between each specimen was not significant.


Declaration of conflicting interests

The author(s) declared no potential conflicts of interest with respect to the research, authorship, and/or publication of this article.

Funding

The author(s) disclosed receipt of the following financial support for the research, authorship, and/or publication of this article: This work was supported by grants from the National Natural Science Foundation of China (Nos 51735003 and 51475094).

ORCID iD

Hongjian Wang  <https://orcid.org/0000-0002-5180-0054>

References

1. Karmakar B. Functional bulk metallic glasses. In: Karmakar B (ed.) *Functional glasses and glass-ceramics*. Oxford: Butterworth-Heinemann, 2017, p. 365, <http://dx.doi.org/10.1016/B978-0-12-805056-9.00012-X>
2. Li HF and Zheng YF. Recent advances in bulk metallic glasses for biomedical applications. *Acta Biomater* 2016; 36: 1–20.
3. Li WH, Chana KC and Xia L. Thermodynamic, corrosion and mechanical properties of Zr-based bulk metallic glasses in relation to heterogeneous structures. *Mater Sci Eng A* 2012; 534: 157–162.
4. Zhou W, Hou J and Weng W. Microstructure, thermal stability and mechanical properties of Zr-Cu-Al-Sn bulk metallic glass. *J Non-Crystal Solid* 2015; 429: 208–212.
5. Liu LH, Ma J and Yu CY. Determination of forming ability of high pressure die casting for Zr-based metallic glass. *J Mater Process Tech* 2017; 244: 87–96.
6. Horton J and Parsell D. Biomedical potential of a zirconium-based bulk metallic glass. *MRS Proc* 2002; 754: CC15.
7. Lin CH, Huang CH and Chuang JF. Simulated body-fluid tests and electrochemical investigations on biocompatibility of metallic glasses. *Mater Sci Eng C* 2012; 32: 2578–2582.
8. Li TH, Wong PC and Chang SF. Biocompatibility study on Ni-free Ti-based and Zr-based bulk metallic glasses. *Mater Sci Eng: C* 2017; 75: 1–6.
9. Hua T, Yang C and Lin S. Biodegradable stents for coronary artery disease treatment: recent advances and future perspectives. *Mater Sci Eng C* 2018; 91: 163–178.
10. Wang G, Fan HB and Huang YJ. A new TiCuHfSi bulk metallic glass with potential for biomedical applications. *Mater Design* 2014; 54: 251–255.
11. Dancer SJ, Stewart M and Coulombe C. Surgical site infections linked to contaminated surgical instruments. *J Hosp Infect* 2012; 81: 0231–0238.
12. Atar-Froyman L, Sharon A and Weiss EI. Anti-biofilm properties of wound dressing incorporating nonrelease polycationic antimicrobials. *Biomaterials* 2015; 46: 141–148.
13. Martin ML, Pfaffen V, Valenti LE, et al. Albumin bio-functionalization to minimize the Staphylococcus aureus adhesion on solid substrates. *Colloid Surf B: Biointer* 2018; 167: 156–164.
14. Ivanova K, Bassegoda A, Tzanov T, et al. Antibacterial coatings on medical devices. In: Tiwari A (ed.) *Handbook of Antimicrobial Coatings*. New York: Elsevier, 2018, pp. 487–507, <http://dx.doi.org/10.1016/B978-0-12-811982-2.00021-4>
15. Campoccia D, Montanaro L and Arciola CR. A review of the biomaterials technologies for infection-resistant surfaces. *Biomaterials* 2013; 34: 8533–8554.
16. Desrousseaux C, Sautou V and Descamps S. Modification of the surfaces of medical devices to prevent microbial adhesion and biofilm formation. *J Hosp Infect* 2013; 85: 87–93.
17. Bagherifard S, Hickey DJ and de Luca AB. The influence of nano-structured features on bacterial adhesion and bone cell functions on severely shot peened 316L stainless steel. *Biomaterials* 2015; 73: 185–197.
18. Bruzard J, Tarrade J and Celia E. The design of superhydrophobic stainless steel surfaces by controlling nanostructures: a key parameter to reduce the implantation of pathogenic bacteria. *Mater Sci Eng C* 2017; 73: 40–47.
19. Meier M, Dubois V and Seeger S. Reduced bacterial colonisation on surfaces coated with silicone nano-structures. *Appl Surf Sci* 2018; 459: 505–511.
20. Hajjaji A, Elabidi M, Trabelsi K, et al. Bacterial adhesion and inactivation on Ag decorated TiO₂-nanotubes under visible light: effect of the nanotubes geometry on the photocatalytic activity. *Colloid Surf B: Biointer* 2018; 170: 92–98.
21. Wang Z, Su Y and Li Q. Researching a highly anti-corrosion super-hydrophobic film fabricated on AZ91D magnesium alloy and its anti-bacteria adhesion effect. *Mater Charact* 2015; 99: 200–209.
22. Choi M, Xiangde L and Park JH. Superhydrophilic coatings with intricate nano-structure based on biotic materials for antifogging and antibiofouling applications. *Chem Eng J* 2017; 309: 463–470.
23. Yuan Y, Hays MP and Philip R. Surface characteristics influencing bacterial adhesion to polymeric substrates. *RSC Adv* 2017; 7: 14254–14261.
24. Oekermann T, Yoshida T and Nakazawa J. Wall thickness and charge transport properties of nano-honeycomb TiO₂ structures prepared by photoetching. *Electrochim Acta* 2007; 52: 4325–4333.
25. Vadillo-Rodríguez V, Guerra-García-Mora AI, Perera-Costa D, et al. Bacterial response to spatially organized

- microtopographic surface patterns with nanometer scale roughness. *Colloid Surf B: Biointer* 2018; 169: 340–347.
26. Courvoisier F, Stoian R and Couairon A. Ultrafast laser micro and nano-processing with nondiffracting and curved beams. *Optic Laser Technol* 2016; 80: 125–137.
 27. Burns SR, Gregg JM and Nagarajan V. Nano-structuring ferroelectrics via focused ion beam methodologies. *Adv Function Mater* 2016; 26: 8367–8381.
 28. Wang L, Chen W and Terentjev E. Effect of micro-patterning on bacterial adhesion on polyethylene terephthalate surface. *J Biomater Appl* 2014; 29: 1351–1362.
 29. Krsko P, Kaplan JB and Libera M. Spatially controlled bacterial adhesion using surface-patterned poly (ethylene glycol) hydrogels. *Acta Biomater* 2009; 5: 589–596.
 30. Sugioka K. Ultrafast laser processing of glass down to the nano-scale. In: Miotello A and Ossi PM (eds.) *Laser-Surface Interactions for New Materials Production*. Berlin: Springer, 2010, pp. 279–293.
 31. Lei Y, Zhang N, Yang J, et al. Femtosecond laser eraser for controllable removing periodic microstructures on Fe-based metallic glass surfaces. *Optic Express* 2018; 26: 5102–5110.
 32. Shaikha S, Singh D and Subramanian M. Femtosecond laser induced surface modification for prevention of bacterial adhesion on 45S5 bioactive glass. *J Non-Crystal Solid* 2018; 482: 63–72.
 33. Cunha A, Elie AM and Plawinski L. Femtosecond laser surface texturing of titanium as a method to reduce the adhesion of *Staphylococcus aureus* and biofilm formation. *Appl Surf Sci* 2016; 360: 485–493.
 34. Franco A and Romoli L. Characterization of laser energy consumption in sintering of polymer based powders. *J Mater Process Tech* 2012; 212: 917–926.
 35. Wang Y, Li Y, Wang Q, et al. Synthesis and evaluation of properties of N, N -bis(perfluorooctyl)imine acetate sodium as a gas-wetting alteration agent. *RSC Adv* 2018; 15: 7924–7931.
 36. Barcikowski S, Hahn A and Kabashin AV. Properties of nanoparticles generated during femto- second laser machining in air and water. *Appl Phys A* 2007; 87: 47–55.
 37. Maragkakia S, Derrien TJY and Levy Y. Wavelength dependence of picosecond laser-induced periodic surface structures on copper. *Appl Surf Sci* 2017; 417: 88–92.
 38. Saghebfar M, Tehrani MK and Darbani SMR. Femtosecond pulse laser ablation of chromium: experimental results and two-temperature model simulations. *Appl Phys A* 2017; 123: 28.
 39. Hori K and Matsumoto S. Bacterial adhesion: from mechanism to control. *Biochem Eng J* 2010; 48: 424–434.
 40. Blesa MA, Weisz AD and Morando AJ. The interaction of metal oxide surfaces with complexing agents dissolved in water. *Co-ordinat Chem Rev* 2000; 196: 31–63.
 41. Azeredo J, Visser J and Oliveira R. Exopolymers in bacterial adhesion: interpretation in terms of DLVO and XDLVO theories. *Colloid Surf B: Biointer* 1999; 14: 141–148.
 42. Gusnaniar N, Van Der Mei HC and Qu W. Physico-chemistry of bacterial transmission versus adhesion. *Adv Colloid Interface Sci* 2017; 250: 15–24.
 43. Soni KA, Balasubramanian AK, Beskok A, et al. Zeta potential of selected bacteria in drinking water when dead, starved, or exposed to minimal and rich culture media. *Current Microbiol* 2008; 56: 93–97.
 44. Decuzzi P and Ferrari M. Modulating cellular adhesion through nanotopography. *Biomaterials* 2010; 31: 173–179.
 45. Luan Y, Liu S, Pihl M, et al. Bacterial interactions with nano-structured surfaces. *Curr Opin Colloid In* 2018; 38: 170–189.
 46. Lau PCY, Dutcher JR, Beveridge TJ, et al. Absolute quantitation of bacterial biofilm adhesion and viscoelasticity by microbead force spectroscopy. *Biophys J* 2009; 96: 2935–2948.
 47. Vassallo E, Pedroni M and Silveti T. Bactericidal performance of nano-structured surfaces by fluorocarbon plasma. *Mater Sci Eng C* 2017; 80: 117–121.